The DOI for this manuscript is doi: 10.1175/JPO-D-13-0121.1

The final published version of this manuscript will replace the preliminary version at the above DOI once it is available.

If you would like to cite this EOR in a separate work, please use the following full citation:

Thomsen, S., C. Eden, and L. Czeschel, 2013: Stability analysis of the Labrador Current. J. Phys. Oceanogr. doi:10.1175/JPO-D-13-0121.1, in press.

Stability analysis of the Labrador Current

Sören Thomsen[1,2], Carsten Eden[1*] and Lars Czeschel[1]

[1] Institut für Meereskunde, KlimaCampus, Universität Hamburg, Germany

[2] Helmholtz Centre for Ocean Research (GEOMAR), Kiel, Germany

October 24, 2013

* *Corresponding author address:* Carsten Eden, Institut für Meereskunde, Universität Hamburg, Germany.

E-mail: carsten.eden@zmaw.de. Tel.: +49 40 42838 7623 Fax: +49 40 42838 2995

Abstract

Mooring observations and model simulations point to an instability of the Labrador Current (LC) during winter, with enhanced eddy kinetic energy (EKE) at periods between 2 to 5 days, and much less EKE during other seasons. Linear stability analysis using vertical shear and stratification from the model reveals three dominant modes of instability in the LC:

- a balanced interior mode with along-flow wavelengths of about 30–45 km, phase velocities of 0.3 m/s, maximal growth rates of $1\,\mathrm{d}^{-1}$ and surface intensified, but deep reaching amplitudes,
- a balanced shallow mode with along-flow wavelengths of about 0.3–1.5 km, about three times larger phase speeds and growth rates, but amplitudes confined to the mixed layer (ML),
- and an unbalanced symmetric mode with largest growth rates, vanishing phase speeds and along-flow structure, and very small cross-flow wavelengths, also confined to the ML.

Both balanced modes are akin to baroclinic instability, but operate at moderate to small Richardson numbers Ri with much larger growth rates as for the quasi-geostrophic limit of $Ri \gg 1$. The interior mode is found to be responsible for the instability of the LC during winter. Weak stratification and enhanced vertical shear due to local buoyancy loss and the advection of convective water masses from the interior result in small Ri within the LC, and to three times larger growth rates of the interior mode in March compared to summer and

fall conditions. Both the shallow and the symmetric mode are not resolved by the model, but it is suggested that they might also play an important role for the instability in the LC and for lateral mixing.

1. Introduction

The Labrador Sea (LS) is one of few places in the world ocean where deep open ocean convection up to 2000 m occurs (Lazier 1973; Marshall and Schott 1999). Extreme cold and dry winter storms over the LS lead to enhanced air-sea buoyancy fluxes and thus to the formation of deep mixed layers (ML). During these events Labrador Sea Water (LSW) is formed, which is the upper part of the North Atlantic Deep Water and an important constituent of the meridional overturning circulation (MOC). Since the MOC in the Atlantic Ocean is responsible for a considerable northward heat transport, the LS is a key region for the global climate system. Atmospheric trace gases such as CO_2 are also taken up and exported southward by the LSW, which makes the LS important for the ventilation of the abyssal ocean as well. The near-surface circulation of the LS is part of the cyclonic subpolar gyre of the North Atlantic and can be decomposed into the West Greenland Current, the Irminger Current and the Labrador Current (LC). We focus here on the LC which is sometimes divided into three different main branches (Lazier and Wright 1993; Cuny et al. 2002). There is a more baroclinic part located at the shelf break, which here will be referred to as the shelf break LC. Another branch is referred here to as the deep LC, which is located further offshore over the continental slope. Finally, there is also a third branch of the LC, located over the shallow shelf.

The classical LSW is formed in the interior LS during deep convection (Schott et al. 2004; Yashayaev et al. 2007). However, recent observational studies suggest that deep convection near the boundary current also contributes significantly to the LSW formation (Lavender et al. 2002; Pickart et al. 2002; Cuny et al. 2005; Palter et al. 2008; Spall 2010). Pickart et al. (2002) find ML depths down to 1400 m over the continental slope within the deep LC during a hydrographic cruise in March 1997. Brandt et al. (2007) discuss the ventilation and transformation of LSW as well as its export in the deep LC. Their modeling study is consistent with observational studies and reveals that the deep LC is an important water mass transformation area due strong buoyancy fluxes during winter. Brandt et al. (2007) estimate that one third of the LSW transformation occurs within the deep LC and is already exported during the ongoing convection period, while the export of the classical LSW from the interior takes several years (Lazier et al. 2002). Thus, the deep LC might provide the most rapid export route of newly formed LSW out of the convection region and a direct communication route between subpolar regions and the subtropical gyre (Schott et al. 2004).

Enhanced eddy kinetic energy (EKE) along the LC is found during the period of water mass transformation within the LS in winter, pointing towards an important role of the unstable boundary current for the ventilation process (Spall 2010). Brandt et al. (2004) find a distinct annual cycle in EKE estimates from satellite altimetry data from 1997-2001 in the LS region along the LC with a maximum of EKE in winter and a minimum in autumn. Morsdorf (2001) analyzes moored current data focussing on velocity fluctuations with synoptic timescales within the LC, and also finds a maximum of EKE in wintertime. Local high-frequency wind forcing, which is strongest during late winter, is sometimes suggested as the source of the velocity fluctuations (e.g. White and Heywood 1995). However, enhanced

EKE along the LC during winter is also found in a high-resolution ocean model simulation forced with monthly mean wind fields (Eden and Böning 2002). This points towards an internal instability process as the source of the velocity fluctuations. Accordingly, Eden and Böning (2002) find enhanced transfer rates of mean potential energy to EKE and a maximum of the cross-stream in situ density gradient in the LC during winter, therefore suggesting baroclinic instabilities as the source of the seasonal cycle in EKE.

Different instability mechanisms can operate in the ocean, depending on the specific background flow and stratification (e.g. Eady 1949; Stone 1966, 1970; Haine and Marshall 1998; Boccaletti et al. 2007): Gravitational instability and (normal) upright convection occurs if a resting, horizontally stratified ocean experiences spatially homogeneous surface buoyancy loss. The resulting convective overturning process generates a deepening ML depth and takes place in convective cells (plumes) with lateral scales of $L = O\,(1\,\mathrm{km})$ for deep convection in the ocean. Depending on the duration and strength of the buoyancy loss, maximum convection depths down to 2000 m can be reached in the LS (Marshall and Schott 1999).

Pure centrifugal or inertial instability occurs for the case of constant density and a zonal background flow without vertical but with meridional shear. A necessary condition for inertial instability is $f < \partial u/\partial y$; where f is the Coriolis parameter, but it is rarely found in this form in the ocean. More often a combination of horizontal and vertical shear is present, for which negative absolute potential vorticity (times f) becomes a necessary condition for symmetric instability (Haine and Marshall 1998; Olbers et al. 2012), which is equivalent to a Richardson number[1] Ri smaller than one. This condition can hold for small f near the

[1]The Richardson number Ri, the ratio of vertical stratification and vertical shear, is defined by $Ri =$

equator or for weak but statically stable stratification and large lateral density gradients. In the ocean the latter situation is frequently present in the ML at frontal zones as for instance in the LC as discussed below; a combination of symmetric instability with gravitational instability leads to slantwise convection (e.g. Haine and Marshall 1998; Olbers et al. 2012). For a flow in the zonal direction, the growth rate of symmetric instability increases with increasing meridional wave number until it reaches asymptotically a fixed value for large l. The growth rate decreases with increasing Ri until it becomes zero for $Ri = 1$. For $Ri < 1/4$, the necessary condition for the familiar Kelvin-Helmholtz instability is met.

For $Ri > 3/4$, baroclinic instability begins to dominate all other instabilities. It is a vertical shear instability taking its energy from the available potential energy of the background flow and feeding it to EKE. Eady (1949) discusses analytical solutions of baroclinic instability for vertically constant shear and stratification and a constant Coriolis parameter f in the quasi-geostrophic limit of large Richardson numbers Ri and small Rossby number[2] Ro. Despite the ad hoc simplifications, Eady's growth rates estimated from observations are well correlated with EKE (e.g. Treguier et al. 1997; Smith 2007; Chelton et al. 2007). The fastest growing wave for Eady's case is found at $kNh/f \simeq 1.6$, where k is the lateral wave number, h the depth scale and N the vertical stratification.

The non-geostrophic baroclinic instability problem allowing for small Ri and finite Ro was first discussed by Stone (1966, 1970) using hydrostatic approximation and by Stone

---

N^2/S^2, with the Brunt-Väisälä frequency $N = \sqrt{-(g/\rho_0)\,\partial\rho/\partial z}$, the (neutral) density ρ, a constant reference density ρ_0, and the vertical shear $S = \sqrt{(\partial u/\partial z)^2 + (\partial v/\partial z)^2}$.

[2]The Rossby number Ro describes the ratio of inertial to Coriolis force terms, defined by $Ro = U/(fL)$, where U is a typical horizontal velocity and L a typical horizontal length scale, and is equivalent to $Ro = \zeta/f$, where ζ is the relative vorticity.

(1971) using non-hydrostatic equations, showing that the results from Eady (1949) can be transferred qualitatively to the situation with small Ri when applying small modifications: The growth rate ω of the fastest growing mode is then given by $\omega^2 \approx 0.09\, f^2/(1+Ri)$, while Eady found $\omega^2 \approx 0.09\, f^2/Ri$, which leads to time scales of about weeks or months for large Richardson numbers as in the classical mesoscale regime. However, for $Ri = O(1)$ the time scales become much shorter and are of $O(1/f)$. Another difference to Eady's case at large Ri is a shift of the maximal growth rate towards smaller wave numbers.

Molemaker et al. (2005) point out that the instability analysis at $Ri = O(1)$ reveals two distinct baroclinic instability modes: The first one is a geostrophically balanced mode, which has the largest growth rates. This mode might be called the classical geostrophic or Eady mode since even for small Ri the simple Eady solution is only quantitatively modified, but not qualitatively. The second mode is a non-geostrophic mode, which has smaller growth rates compared to the geostrophic mode, but might play an important role for the dissipation of kinetic energy of the mean balanced flow (Molemaker et al. 2005, 2010). The geostrophic mode is well captured by the hydrostatic equations whereas the non-geostrophic mode has a large non-hydrostatic component (Stone 1971). Some authors (e.g. Boccaletti et al. (2007)) call the balanced geostrophic mode at small Ri "ageostrophic baroclinic instability", which is misleading (Thomas et al. 2008) since it is still geostrophically balanced.

Mixed Layer Instabilities (MLI) are a special type of baroclinic instability at low Ri and are trapped in the ML, if a large change in density separates the ML from the more stratified interior. Strong lateral density gradients in weakly stratified MLs can lead to this kind of instability. Boccaletti et al. (2007) show that these types of instabilities have length scales close to the Rossby radius characteristic for the ML defined as Nh/f, where N represents the weak stratification in the ML of depth h. For typical ML properties (e.g. $N = 10^{-3}\,\mathrm{s}^{-1}$, $h = 100\,\mathrm{m}$ and $f = 10^{-4}\,\mathrm{s}^{-1}$) this results in lateral scales of $O(1\,\mathrm{km})$, which is the typical length scale of the so-called "submesoscale" flow in the surface of the ocean (Munk et al. 2000). Furthermore, the MLI can be important for the restratification of the ML.

The objective of this study is to learn about the frontal instability process along the LC, i.e. which kind of instability is at work here. In particular, we answer the question: Why do we observe the enhanced EKE levels in the LC only during late winter? High-resolution ocean model simulations and observational current data are evaluated to answer the question; linear stability analysis is applied to understand the physics of the frontal instability processes occurring within the LC. Understanding the instability process within the LC is crucial, as it might be important for mixing processes, which alter the water mass properties of the newly formed LSW during its rapid export within the deep LC (Spall 2010), and since the transformation rate might be a controlling factor of the Atlantic MOC and the meridional heat transport. Coarse-resolution ocean models and climate models do not resolve these processes and even most high-resolution ocean models are not able to simulate the enhanced EKE along the LC during late winter (Treguier et al. 2005). Furthermore it is important to understand the processes in order to parametrize their effects in coarse-resolution ocean and climate models.

This paper is structured as follows: In section 2, the model and observational data are described. The seasonal cycle of EKE within the model and observational datasets is presented in section 3. The method and the results of the linear stability analysis are presented in section 4. The oceanic background conditions within the LC are analyzed in section 5 in order to explain the seasonality of the instability process and the EKE. The results are summarized and discussed in section 6.

2. Model and observations

a. Numerical model simulation

An ocean general circulation model of the North Atlantic is analyzed in this study, with lateral resolution of $1/12^o$, which is about 5×5 km in the LS, and 45 vertical levels with thicknesses increasing from 10 m at the surface to 250 m at depth. The model has already been used for several different studies concerning the LS: Eden and Böning (2002) analyse the EKE as well as the strength and position of the boundary currents in the LS, which are in good agreement with observations. The model version of this study is the same as the one analyzed in Brandt et al. (2007), discussing the ventilation, transformation and export of LSW in the deep LC. We call this model simulation hereafter FLAME. Another more recent model version with very similar configurations as FLAME but using the Massachusetts Institute of Technology General Circulation Model code (Marshall et al. 1997) is also analyzed and is called accordingly MITGCM.

FLAME and MITGCM share identical horizontal and vertical resolution as well as the same bathymetry. The monthly mean climatological surface forcing is also the same and identical to Eden and Böning (2002); it is derived from a three-year long analysis of the European Centre for Medium-Range Forecasts (ECMWF) operational forecast model by Barnier et al. (1995), with a surface heat flux formulation following Haney (1971) and surface salinity relaxation towards the monthly mean climatology of Levitus and Boyer (1994) with a time scale of 30 days. All results shown here are taken from integrations following a 10 year spinup phase starting from rest and temperature and salinity given by Levitus and Boyer (1994). Open lateral boundaries following Stevens (1990) are applied at the southern (20^o S) and northern edge (70^o N) of the model domain, and a relaxation zone towards the initial conditions within the Mediterranean Sea.

The main differences between FLAME and MITGCM are the following: The primitive equations are discretized on a C-grid in MITGCM instead of a B-grid in FLAME, and a free-slip boundary condition is used in MITGCM instead of no-slip in FLAME. The biharmonic viscosity in FLAME is $2 \times 10^{10}\,\mathrm{m^4 s^{-1}}\,\cos\phi$, where ϕ denotes latitude, while in MITGCM a constant biharmonic viscosity of $10^{10}\,\mathrm{m^4 s^{-1}}$ is used. We use biharmonic mixing in MITGCM with the diffusivity identical to the viscosity, while in FLAME harmonic isopycnal mixing with a diffusivity of $50\,\mathrm{m^2/s}$ is applied. In FLAME, a bottom boundary layer parameterization following Beckmann and Döscher (1997) is applied, but not so in MITGCM. A simple surface mixed layer scheme after Kraus and Turner (1967) is used in FLAME, while we use the mixed layer model by Gaspar et al. (1990) in MITGCM.

FLAME shows improvements of the hydrographic properties compared to the older simulations (Czeschel 2005; Brandt et al. 2007). The simulated maximum convection depth within the interior LS (Lavender et al. 2002) seems to be more realistic in FLAME, while other high-resolution ocean models often suffer from unrealistic shallow or deep convection depths (Treguier et al. 2005; Rattan et al. 2010). In Czeschel (2005) and the other references mentioned above, the reader can find more information about model details and the improvements of the hydrographic properties and deep convection. In MITGCM, however, the maximum convection depth is again too deep within the interior LS (not shown). The reason for this bias is currently under investigation; the missing bottom boundary layer model in MITGCM and the missing deep inflow of very dense water masses might be an explanation.

We use two different model configurations in this study for the following reasons. First, only daily averages of one year have been archived for FLAME which permits the comparison with spectral properties of mooring current observations on time scales of days (see below), and limits the discussion concerning the seasonality of the signal. Second, we use MITGCM as a sensitivity experiment to test whether the features we discuss here are consistent or sensitive to small details of the model configuration. We will discuss the differences between FLAME and MITGCM with respect to the annual cycle of EKE and the linear stability below in more detail.

b. *Observations*

In addition to the model simulations, we also discuss near-surface velocity measurements from moored acoustic doppler current profilers (mADCP) and a moored rotor current meter (RCM) located in the LC near the exit of the LS. Three moorings are used, with positions as marked in Fig. 1. Two moorings (K7 and K8) are located near 53^oN within the LC. K7 is closer to the shelf break, while K8 is located further offshore. Another mooring (K6) is located further upstream in the center of the LC near 55^oN. The mADCPs at K7 and K8 are upward looking at the top of the mooring line and have an instrument depth of 344 m and 324 m, respectively. Other instruments from both moorings are not discussed here. The dataset from K7 and K8 covers 2 years (1997-1999) and is available at an hourly frequency. A more detailed description of the mooring configuration of K7 and K8 can be found in

Fischer et al. (2004). In addition to K7 and K8 we use one year (1996/1997) of mADCP and RCM data at an hourly frequency at K6. The ADCP at K6 is also upward looking at an instrument depth of 350 m. Here, we also use an RCM located at 662 m depth. A more detailed description of the mooring configuration of K6 can be found in Cuny et al. (2005).

3. Annual cycle of EKE in the Labrador Current

Fig. 1 shows the annual mean pattern of EKE within the LS, as simulated by MITGCM. A large maximum of EKE can be found at the continental slope of West Greenland reaching into the interior LS with values exceeding 300 cm^2/s^2 near the coast. The EKE in the interior LS reaches values between 100 cm^2/s^2 and 150 cm^2/s^2. Another weaker maximum with values between 50 cm^2/s^2 and 100 cm^2/s^2 is found along the LC. This pattern of EKE in the LS is very similar in each year of our climatologically forced simulations with slightly different amplitudes. Year-to-year differences in EKE in the LC remain smaller than 20 cm^2/s^2.

The spatial pattern of EKE in the LS is very similar to that in FLAME, which is described in detail by Eden and Böning (2002). However, there are some differences in the absolute values: Eden and Böning (2002) find larger EKE of about 250 cm^2/s^2 to 400 cm^2/s^2 in the interior LS and values up to 150 cm^2/s^2 along the LC. A detailed comparison of FLAME with observational estimates of transports and EKE can be found in Eden and Böning (2002). It turns out that FLAME tends to overestimate the EKE maxima compared to estimates based on satellite altimeter data. This would suggest that MITGCM is closer to the observations in this respect, but we note that altimeter-based EKE estimates tend to be lower than estimates based on surface drifter data (Fratantoni 2001). Furthermore, large interannual variability in the LS complicates the comparison with our climatologically forced model simulations.

Fig. 2 shows the monthly mean EKE at K6 from MITGCM, FLAME and the moored current data. All three datasets show a clear peak of enhanced EKE in March and a strong surface intensification. Maxima of about $100\,\mathrm{cm}^2/\mathrm{s}^2$ are reached in both model simulations at 100 m depth during March, where K6 shows larger values of up to 250 $\mathrm{cm}^2/\mathrm{s}^2$. A second maximum during summer shows up in K6. It is not as strong in the near surface waters with values of about $100\,\mathrm{cm}^2/\mathrm{s}^2$ but reaches to greater depths. FLAME also simulates a second smaller maximum, which is separated from the maximum during March, while in MITGCM the EKE slowly decreases during spring until it reaches minimal values in late autumn so that a second maximum in summer cannot be identified.

EKE is highly variable during different years in the observations (not shown), such that, in principle a longer time series is needed for a more reliable comparison. However, our analysis already suggests that the models generally simulate lower EKE compared to the observations. Estimates of EKE along the LC from satellite measurement also generally are larger compared to the model simulation (Brandt et al. 2004). This low bias of EKE in the model simulations might be explained by the missing high-frequency wind forcing in the model simulations, which would add additional variability into the current field during the whole year. Another possibility is a missing instability mechanism due to lack of grid resolution or excessive numerical damping. However, a more detailed analysis of this low bias is beyond the scope of the present paper; we assume that the bias does not effect the results presented here. Since both models show a distinct annual cycle in EKE with the same timing and similar maxima as the observational estimates (see Fig. 2), we are confident that our assumption is justified. In any case, the model simulations are forced with monthly mean winds. Consequently, as already pointed out by Eden and Böning (2002) internal flow instabilities are suggested as the main source of enhanced EKE during winter and not high-frequency wind as suggested by e.g. White and Heywood (1995) and Morsdorf (2001).

Fig. 3 shows spectral estimates from the current data of the three different moorings and from 3 years of MITGCM for different seasons. While 6-hourly snapshots are available for the spectral estimates in MITGCM, the archived daily averages of only one year for FLAME permit the detailed spectral analysis here. At K6 (Fig. 3 a,d), which is the northernmost mooring (see Fig. 1), the spectral estimate shows enhanced variance near the 2- and the 8-day-period during winter. In spring, the peaks are shifted towards longer periods associated with a strong increase of variance at the 10-day-period. During summer and autumn, most of the variance can be found at longer periods around 10 days. The spectra of the model simulation at K6 also show enhanced variance during winter between 2- to 8-day-periods as well as a shift towards longer periods in spring. During winter, the highest variance can be found near the 2-day-period. The peak is, however, not as large as in the observational data. In summer, the spectra of the model data contain less energy with enhanced variance between 5 to 10 days, while in autumn, almost no high-frequency variance can be found in the model simulation. This is in contrast to the observations, where high-frequency variability is also present during these seasons, and might be related to the missing high-frequency wind forcing of the model simulations, and/or a missing instability mechanism.

The spectrum of K7 (see Fig. 3 b,e), which is located at the exit of the LS at around 53^o N, shows a maximum at the 5-day-period for winter. During the rest of the year most of the variance is contained at longer periods between 5 and 10 days. The spectra of the simulation show a similar behavior during winter and spring; in winter, most of the energy is found at periods of 5 days. As seen before, amplitudes are in general lower in the model. The position of K8 (see Fig. 3 c,f) is located further offshore than the position of K7. The spectra of K8 show enhanced variance between 5 and 10 days during winter, while the spectra of the model simulation show a distinct peak at a period of 5 days during winter. Similar to K8, less energy is found in the model data during the rest of the year.

The spectral analysis at 300 m depth (not shown) generally reveals lower energy levels compared to the surface. Model and observations agree at K7 and K8, showing enhanced high-frequency variance during winter at a period of 5 days. K6 also shows enhanced variance near a period of 2 days, which cannot be found in the model. However, the model also shows enhanced variance during winter. As seen before, the model simulation contains much less energy compared to the mooring data, especially at longer periods.

We made no attempt to test the statistical significance of the individual spectral estimates, and we doubt that any of them are on the basis of a restrictive null hypothesis given the short time series. Therefore, Fig. 3 represents only a qualitative analysis of the high-frequency variability comparison of the energy levels in the model and the observations. Nevertheless our qualitative spectral analysis suggests that in general most of the high-frequency variance occurs during winter. At all moorings the ADCP data show enhanced variance at periods between 5 to 2 days, which points to processes with very short time scales. In general, the spectra of the model and the observational data are similar in late winter. However, some differences also exist. The most striking difference in spectral behavior occurs in autumn. Almost no high-frequency variance is found in the model data but enhanced variance near the 10-day-period shows up in the observations. In summer the difference is not as strong (but also present) especially at K7 and K8 which are further south. We speculate that the missing variance in summer and autumn in the model simulation might be related to the missing high-frequency wind forcing in the model, which would add additional variability into the current field during the whole year, and/or to a missing instability process in the model.

The simulations demonstrate that the high-frequency velocity fluctuations in winter are associated with a simultaneous instability of the whole LC: Fig. 4 shows speed and velocity of the upper LC at a depth of 91 m at four different times (of the year) from MITGCM. Similar structures can be seen in FLAME as shown by Eden and Böning (2002) in their Fig. 8. The speed along the shelf break LC north of the Hamilton Bank at 55^oN and between 56^oW and 54^oW is relatively constant in mid December ranging between 0.6 m/s and 0.7 m/s . The snapshot in mid March reveals a different picture: The LC becomes unstable and small scale velocity fluctuations are present in the whole LC. The absolute velocity is highly variable in the area of the LC and reaches values between 0.1 m/s and 1 m/s. The snapshot in mid June reveals a reorganizing of the upper shelf break LC. In mid September absolute velocities reach 0.5 m/s and the LC is slightly broader than in mid June. In FLAME the LC exhibits a similar behavior.

The instabilities start to grow at the offshore edge of the shelf break LC when convective water masses appear in the boundary current (not shown). The first wave-like disturbances can be seen very quickly with timescales O(days) and along-stream wavelengths of about $30-40$ km. A wave passes a particular point in the LC within about two days. The enhanced variance near the two-day period, which can be found in the spectra, can be associated with these small scale disturbances. However, a further analysis of the time evolving flow field reveals that frontogenesis sets in rapidly leading to non-linear characteristics of the flow. Frontal strain and shear rapidly deform the growing waves and consequently different wavelengths develop. An upscale energy transport seems to generate larger lateral scales with longer periods further downstream. This is supported by the spectral estimates of the model current data, which reveal that at the northernmost mooring K6, shorter timescales are generally found compared to the moorings further downstream.

4. Linear stability analysis of the Labrador Current

In this section, we discuss a non-hydrostatic ageostrophic linear stability analysis similar to the one performed by Stone (1971). However, the discussion here is slightly more realistic, since we also account for the vertical variation of the background shear and stratification, for the horizontal components of the Coriolis force, and apply a β-plane approximation rather than a f-plane. Assumptions, and the mathematical and numerical details of our method are described in the appendix. Our linear stability analysis predicts the characteristics of perturbations on a vertically sheared background flow (which is taken here as the LC). Vertical eigenfunctions and eigenvalues for a given background flow are estimated numerically based on the linearized Navier-Stokes equations. If the amplitudes of those solutions are growing in time, i.e. when eigenvalues of the solutions become complex, they can be associated with unstable waves. The stability analysis yields time and length scale of the fastest growing wave solution, as well as perturbation quantities such as u' and v', and correlations such as EKE from $(u'^2 + v'^2)/2$. The unstable waves grow exponentially with time and it is assumed that the fastest growing waves will dominate after a short period of time and thus are the ones that can be identified in the model simulation and the observations.

The amplitude of the wave solution is not determined by the linear stability analysis. For the scaling of the amplitude in u and v, the imaginary part of the frequency ω_i of the fastest growing wave is used as the inverse time scale and its wavelength $L = 2\pi/k$ as the spatial scale. It is, however, clear that the final eddy length scale is a result of the non-linear processes excluded from the linear analysis considered here. For geostrophically balanced flow, L is usually larger than the scale of the unstable wave due to an inverse kinetic energy cascade (e.g. Olbers et al. 2012). However, it was shown in Killworth (1997); Eden (2011, 2012); Vollmer and Eden (2013) that the scaling based on the properties of the linear stability analysis yields indeed reasonable eddy amplitudes and related eddy diffusivities for meso-scale flow.

We here use monthly mean values of the model simulations within the LC for different times during the year as the background flow and stratification for the linear stability analysis. We note that the linear stability analysis does not rely on the primitive equations as the model simulation, but is more general, and will thus reveal modes of instabilities which are not permitted in the model. We use the model simulation to provide the background flow and stratification since sufficient observations are not available. We use FLAME instead of MITGCM for the background conditions, since FLAME provides a stratification in slightly better agreement to observations because of the bias in convection depth in MITGCM. The stability analysis of the LC reveals three dominant modes of instability, which we call the interior, the shallow and the symmetric mode. These modes correspond to baroclinic instability in the interior, to baroclinic instability in the mixed layer (both at low Ri), and symmetric instability, respectively, and are discussed in the following.

a. Interior mode

Fig. 5 shows the results of the linear stability analysis for background flow and stratification taken from March mean values of FLAME at the velocity grid point closest to the position of K6 within the LC. We have excluded the top 20 m from the analysis to avoid the ageostrophic Ekman layer. We have also excluded a bottom Ekman layer of the three lowermost grid boxes, in order to stay consistent with the linear stability analysis, where a geostrophically balanced background flow was assumed. The vertical grid which is used to solve the linear stability problem is identical to the model grid.

The speed of the background velocity decays from about 0.6 m/s at 20 m to 0.17 m/s at 700 m. The stratification is weak in the upper 50 m, and increases to $N = 5.4 \times 10^{-3}\,\mathrm{s}^{-1}$ at 55 m and decays with depth to $N = 0.8 \times 10^{-3}\,\mathrm{s}^{-1}$ at 700 m. The growth rate (the imaginary part of the eigenvalue ω) is estimated for different k and l combinations, where k is the zonal and l the meridional wave number. The resulting growth rates for each k and l combination are shown in Fig. 5a). The maximal growth rates are given for an orientation of the wave vector roughly parallel to the background flow, which is indicative of an Eady-type baroclinic instability. The fastest growing mode has a growth rate of $1/0.94\,\mathrm{d}^{-1}$ and a corresponding (rotated, along-flow) wavelength of 42.5 km, thus close to the interior first baroclinic Rossby radius, or zonal and meridional wavelength of 44.8 km and −134.5 km, respectively.

The phase velocity, $c = Re(\omega)/\sqrt{k^2 + l^2}$, of the corresponding wave solutions (given by the real part of the eigenvalue) is shown in Fig. 5b). For the fastest growing mode, the phase velocity is 0.28 m/s, leading to a steering level of the waves (where background flow and opposite phase velocity are identical) at a depth of 330 m depth. Note that isopycnal diffusivities are expected to have a maximum at the steering level (Smith and Marshall 2009; Vollmer and Eden 2013).

The vertical structure function of the perturbation velocities u and v and the resulting EKE are shown in Fig. 5e) and f), respectively, using the scaling of the amplitudes as outlined above. The velocities are surface intensified with maximal values of 0.35 m/s and decay to a mid-depth minimum of 0.15 m/s at depths below 200 m, before increasing slightly again, similar to an Eady-type instability. The EKE shows a surface maximum of $300\,\mathrm{cm}^2/\mathrm{s}^2$ and decays to $50\,\mathrm{cm}^2/\mathrm{s}^2$ below 200 m. Since it shows loadings over the whole water columns, we call this mode the interior mode. It can be characterized as an Eady-type baroclinic (balanced) instability, but at Richardson numbers of $O(1)$ as discussed below.

For the linear stability analysis of the interior mode shown in Fig. 5 we have chosen the same vertical resolution as in the ocean circulation model (see section 2) and found this grid also appropriate for the linear stability analysis. However, sharp gradients in the vertical shear or stratification in the ML (Fig. 6) can lead to unstable modes resulting from grid noise, which are not physically meaningful. In the circulation model, the grid noise modes are damped by lateral and vertical friction and diffusion, which we have also applied in the linear stability analysis (see appendix). The effect of friction and diffusion on the interior mode is small however; the calculations for the interior mode are repeated with friction comparable to the friction used in the model simulations and without friction; changes in growth rates and vertical structure functions are within a few percent. Note that we have also excluded the influence of topography. The possible impact of topography is discussed in the last section.

Table 1 show the growth rates and wavelengths of the interior mode at K6 using monthly mean stratification and shear from FLAME for all months. The interior mode is present year-round, but has its maximum growth rate in March, where we also see the maximum in EKE at K6 both in the observations and the model. From November to February growth rates are also enhanced but smaller than in March, while during the rest of the year, growth rates are much smaller, except for May where a local maximum is present.

The wavelength of the interior mode agrees with a qualitative comparison with the wavelength seen in the model simulation during the initial instability of the LC shown in Fig. 4. From wave length and phase speed, we calculate a wave period of about 1.8 days of the most unstable wave related to the interior mode at K6 in March. This is at least in qualitative agreement to the spectral estimate of velocity fluctuations in both the mooring data and the model simulation, although the spectral estimates show also enhanced variance at larger periods, pointing towards an inverse energy cascade in the turbulent flow. We therefore conclude that the interior mode is responsible for the instability of the LC in the model simulation and speculate that this might also be the case in the observations.

b. *Shallow mode*

For a typical monthly mean profile of background shear and stratification of the shelf break LC, a further mode is present. It is related to the weakly stratified ML, can be characterized as a baroclinic (balanced) mixed layer instability at small Ri, and is called the shallow mode. Fig. 6 shows this shallow mode for January mean values of background flow and stratification taken from FLAME at the velocity grid point closest to the position of K6. Here, we use for the numerical linear stability analysis a higher vertical resolution than for the interior mode of 1 m, i.e. much higher than the vertical resolution of the circulation model. We also restrict the analysis to the upper 200 m of the water column, since repeating the analysis with deeper profiles does not change the shallow mode considered here (compare also Fig. 7). This can be explained by almost vanishing vertical velocities of the shallow mode below the thermocline, such that the (approximate) lower boundary condition $w = 0$ at $z = 200\,\mathrm{m}$ becomes appropriate. The velocity and stratification profiles from the model simulation have also been smoothed with a running mean over a depth range of 12 m, and the linear stability analysis was used without any lateral friction and diffusion. The shear due to ageostrophic Ekman flow in the upper two grid boxes was removed, in order to stay consistent with the linear stability analysis, where a geostrophically balanced background flow was assumed.

Different to the interior mode that exhibits a global maximum of the growth rates in wavenumber space (Fig. 5a), the shallow mode (red cross in Fig. 6a) appears as a saddle point. This is because the Richardson number Ri becomes smaller than one in the mixed layer – as seen in Fig. 6e) – which leads to the existence of symmetric instabilities with larger growth rates than both interior and shallow modes for large cross-flow wavenumbers. We note that applying a threshold to N to prevent Ri smaller than one, eliminates indeed the symmetric mode. The shallow mode becomes a global maximum of the growth rates at an almost identical position in wavenumber space as the red cross in Fig. 6a) (not shown) with, however, slightly smaller maximal growth rates due to the increased Ri. The symmetric mode is discussed in the next section, here we first concentrate on the shallow mode.

The growth rates of the fastest growing shallow mode are $> 3\,\mathrm{d}^{-1}$ in Fig. 6a) and thus larger than the ones of the interior mode. As for the interior mode, the wave vector of the shallow mode is parallel to the background velocity, pointing also to an Eady-type baroclinic instability, but the along-flow wavelength of the shallow mode is $O(1\,\text{km})$, i.e. much smaller than the one of the interior mode. The lateral scale of the shallow mode is close to the ML deformation radius, defined as $N_{ml}h_{ml}/f$, where N_{ml} and h_{ml} are the stability frequency within the mixed layer and the mixed layer depth, respectively.

The phase velocity of the shallow mode is 0.56 m/s, i.e. much faster than the one of the interior mode. In contrast to the interior mode, the velocity amplitudes of the shallow mode show loadings almost exclusively in the ML, but have – because of the much smaller lateral scale – maximal amplitudes of only 0.08 m/s, i.e. much smaller than those associated with the interior mode. Since the wavelength of the shallow mode is smaller than the horizontal resolution of the model, the shallow mode cannot be found in the model simulations and consequently cannot be responsible for the instability of the LC in the simulations. However, it is suggested that it will show up by increasing the model resolution and might also play an important role for the instability process in the real ocean.

The interior mode is also present in Fig. 6a) at similar wave numbers and with similar vertical eigenfunctions as for March shown in Fig. 5a), but with smaller growth rates than the shallow mode. The interior mode can, however, hardly be seen in Fig. 6a) since for the wave number scaling used in Fig. 6a), the interior mode is located at a local maximum of growth rates very close to zero wave number amplitude. Therefore, we show in Fig. 7 the growth rate as a function of the logarithm of the along-flow wavenumber and for zero cross-flow wavenumber, solving the linear stability problem for March shown in Fig. 5 also at a high vertical resolution of 2 m. Here, both interior and shallow mode can be seen as local maxima of the growth rates, with similar vertical structure in u and v as above.

Table 1 shows that the shallow mode is present year-round at K6, since growth rates are larger than $3\,\mathrm{d}^{-1}$ in almost each month. Different to the interior mode, however, the shallow mode shows no clear annual cycle in its growth rates, and in particular no maximum during late winter. On the other hand, the wavelengths of the shallow mode become larger in winter (November to March) than during the rest of the year, since the mixed layer depth – and thus the Rossby radius representative for the mixed layer – is larger during winter.

c. Symmetric mode

The symmetric mode only shows up in the LC when the Richardson number Ri becomes smaller than one in the ML. Symmetric instabilities can occur if the potential vorticity (times f) becomes negative or for $0 < Ri \leq 1$. Richardson numbers well below one are indeed present in both model simulations within the ML above the shelf break LC especially during early winter when the ML is deeper (see Fig. 6e and also Fig. 9), but also during all other months.

While for the interior and shallow mode the fastest growing modes are found for a wavenumber vector $\boldsymbol{k}$ oriented parallel to the background flow, Fig. 6a) shows that largest growth rates associated with the symmetric mode are given for $\boldsymbol{k}$ oriented in cross-frontal direction. Furthermore, the interior and shallow modes can be found for along-flow wavelengths close to the Rossby radius – either the interior Rossby radius or the Rossby radius representative for the mixed layer – while the symmetric mode is found for very small cross-flow wavelength.

The numerical stability analysis predicts maximum growth rates at the scaled wavenumbers $k = -0.45$ and $l = -1.06$, or $k = 0$ and $l = 1.1$ when rotating the background flow into a zonal direction. Extending the analysis to larger wave numbers as shown in Fig. 6a) and b), the maximal growth rate of the symmetric mode further increases for larger (rotated) l, until it reaches asymptotically its maximum (not shown). The growth rate for the scaled wavenumber $\boldsymbol{k} = (-0.45, -1.06)$ of the symmetric mode is already much larger than those for the interior and the shallow mode, i.e. about $11\,\mathrm{d}^{-1}$ for a rotated meridional wavelength of 310 m. The phase velocity of the symmetric mode tends to vanish, which shows that these solutions are not real waves as for the interior and shallow modes, where the largest growth rates are associated with non-zero phase speeds. Different to the interior and the shallow mode, the symmetric mode also shows no structure in the along-flow direction, and it features very small wavelength in the cross-flow direction. The vertical structure of u and v of the symmetric mode shows maximal values of 3.7 cm/s at 23 m depth and vanishing velocities below the ML base.

For wavelengths comparable to the lateral model resolution of about 5 km in the LS, the linear stability analysis predicts maximal growth rates of the symmetric mode which are much smaller than those of the interior mode, and which are likely damped by the friction in the model. Thus, we do not expect to see the symmetric mode in the hydrostatic model simulations. In the ML of the real LC, however, symmetric instability is likely to be present and will be related to slantwise convection. Note that the circulation model is hydrostatic and consequently not able to simulate slantwise convection.

5. Seasonality of the Labrador Current instability

The interior mode has lateral scales of 30 to 45 km, thus is well resolved by the $1/12^o$ model simulations, while we do not expect to see the symmetric and shallow mode. By applying the local linear stability analysis to monthly mean flow and stratification of the model simulation at each grid point in the LS, the interior mode is shown here to be responsible for the local maximum in EKE along the LC and its seasonality in the model simulations. Fig. 8a,b) shows the growth rates of the interior mode during March and September in the southwestern LS. Maximal growth rates up to $1.5\,\mathrm{d}^{-1}$ are reached in the northern part of the LC in March, while in the interior LS and onshore (except close to the shoreline), growth rates are much smaller or even vanish. Further downstream of the LC, the growth rates reach maximal values of about $1\,\mathrm{d}^{-1}$. In contrast, the growth rates along the LC are about three times smaller in September. Fig. 8c,d) shows the associated EKE during March and September at around 100 m depth. In March, EKE reaches 250 $\mathrm{cm}^2/\mathrm{s}^2$ within the LC, while in September the EKE is much weaker with maximum values of around 50 $\mathrm{cm}^2/\mathrm{s}^2$. Both timing and magnitude of the changes in growth rate and EKE thus agree well with both the model simulation and the observations shown in Fig. 2. Further, the growth rates and the EKE are enhanced along the whole LC in March, in agreement with both model and observations. This suggests that the EKE maximum in late winter is produced locally along the whole LC due to the interior mode, i.e. due to baroclinic (balanced) instability. Wavelengths between 25 and 50 km, i.e. between 1 and 2 times the Rossby radius, are predicted along the LC for the interior mode in March (not shown). This is in good agreement with the first wavelike disturbances found in the model simulation. Note that in March wave numbers are slightly smaller than in September. A shift towards smaller wave numbers points to ageostrophic effects for $Ri = O(1)$, which we indeed find in winter as shown next.

Stratification, vertical shear and the resulting Richardson numbers determine the growth rate of the interior mode. Thus, these variables are discussed here in more detail for the near surface LC to explain the timing of the instabilities. Fig. 9 shows the monthly mean stratification N, vertical shear S as well as the Richardson number Ri along 57.6^{o}N taken from FLAME for different months of the year. The transect is marked in Fig. 1. The seasonal cycle in N, S and Ri is related to the local ML variations and the advection of convective water masses from the interior LS. Due to increasing wind-induced turbulence the ML starts to deepen slightly already in September (not shown). The ML further deepens In October and November, but the water masses below the ML are still strongly stratified resulting in large Richardson numbers $Ri \gg 1$ below the ML. In late winter, however, weak stratification is also found below the ML depth with a maximum value of about $N = 5 \times 10^{-3}\,\mathrm{s}^{-1}$ in March, and no clear pycnocline can be identified anymore, which was present in fall and early winter. This erosion of the pycnocline is caused by a combination of lateral advection of ventilated water and local surface heat fluxes.

Due to the decrease in N in January, and due to an increase in the vertical shear S, the Richardson number $Ri = N^2/S^2$ starts to decrease significantly to values below 10, starting in the upper offshore part of the shelf break LC. Both the decrease in N and the increase is S are related to the approach of ventilated, much denser and weakly stratified waters from the interior LS. The lowest Richardson numbers in the LC can be found in February and March. Due to strong vertical shear and weak stratification in the upper 200 m Richardson numbers well below 10, even close to 1 are reached. In April, the restratification starts due to local surface warming and due to the lateral cross-stream mixing induced by the instabilities. The restratification due to strong positive surface heat fluxes accelerates in March, but Richardson Numbers around 10 are still found in the depth range of 100 m due to the continuing presence of strong vertical shear. Only in late summer and autumn the Richardson numbers are large anywhere in the subsurface LC due to a combination of weak shear and strong stratification. Note that the vanishing N close to the bottom occasionally leads to low Richardson numbers as seen in Fig. 9, however, without any seasonal cycle or consequence on the instabilities of the LC.

As shown above the vertical shear is strongest in the late winter whereas the stratification is weakest in winter. Consequently, both the annual cycle of the vertical shear and stratification are important for the instability process within the LC. Note that there is also an increase of the mean Rossby numbers along the LC in late winter in the model simulations. We have estimated the Rossby number using $|\zeta|/f$, where ζ denotes relative vorticity. Mean maximum values of about 0.1 - 0.2 are reached along the LC in late winter, whereas in September the Rossby numbers are well below 0.1. Rossby numbers larger than 0.3 are found in more than 10% of the grid boxes in March, whereas in late summer and autumn no Rossby numbers larger than 0.3 are found along the LC. Since large Rossby numbers indicate that ageostrophic terms are of larger importance, the results from the quasi-geostrophic approximation are therefore in principle invalid to explain the dynamics of the LC.

6. Summary and discussion

The LC features a local maximum in EKE which is known to have a pronounced annual cycle, peaking during winter and with much lower values during the rest of the year. The dynamical cause of this EKE maximum and its seasonality are the focus of this study. It can be important for lateral mixing and stirring processes, which alter the water mass properties of newly formed LSW during its rapid export within the deep LC, and for the transformation rates of LSW, which might be a controlling factor of the Atlantic MOC and its associated meridional heat transport.

The pronounced annual cycle of EKE along the LC is found both in mooring current data and in high-resolution ocean circulation model simulations. The EKE magnitudes in the model simulations agree qualitatively well with observational estimates, although with a low bias particularly in summer and fall, which we relate to the missing year-round high-frequency wind stress forcing and/or to a missing instability process in the model. Spectral analysis of the mooring current data and velocities from model simulation within the LC show enhanced high-frequency variance for periods between two and five days during the peak in winter. Since the model is driven by monthly mean wind stress, internal instability can be made responsible for the seasonality of the EKE in the LC, while high-frequency wind stress forcing can be excluded as possible driver in the model. A model simulation with high-frequent wind forcing would help to explain and to quantify the missing background level in the variance, which is left for future work.

Using typical stratification and vertical shear of the LC taken from the model simulations, linear stability analysis predicts three dominant modes of instability in the shelf break LC:

- An interior mode with an along-flow wavelength of about 30–45 km comparable to the local interior first baroclinic Rossby radius, and with a phase velocity of about 0.3 m/s. This mode is present year-round, but has a maximal growth rate of about $1\,\mathrm{d}^{-1}$ in March. It is surface-intensified, but with deep reaching amplitudes. The interior mode is akin to baroclinic instability, but operates mainly at low Richardson numbers and finite Rossby numbers, therefore with much larger growth rates than for the quasi-geostrophic limit of $Ri \gg 1$.

- A shallow mode is present year-round, with an along-flow wavelength of about 0.3–1.5 km, comparable to the Rossby radius related to the depth and stratification of the mixed layer, and with a phase velocity of about 0.6 m/s. The amplitudes of the shallow mode are confined to the mixed layer, but it has growth rates about three times larger than the growth rates of the interior mode. The shallow mode is also a balanced mode akin to baroclinic instability, but confined to the mixed layer and for $Ri = O(1)$. It is not resolved by the horizontal grid of the model, but is likely to be present in observations.

- A symmetric mode can be found due to Richardson numbers below one in the ML of the LC with vanishing phase velocity. It has the largest growth rates at small cross-flow wavelengths, but no along-flow structure, and its amplitudes are also confined to the mixed layer. Growth rates of this modes on the grid scale of the model are small and thus not seen in the simulations, but the symmetric mode is likely to show up in the ML of the LC associated to slantwise convection.

The interior mode is found to be in agreement with the growing instabilities in late winter showing up in the model simulations. It has lateral scales close to the local Rossby radius of deformation and is thus resolved in the model. Due to the low Richardson numbers in the LC in winter, the time scale of the interior mode is comparable with the time scale of MLI or "submesoscale" instabilities discussed e.g. by Boccaletti et al. (2007). The rapid start of the instability process along the whole LC in the model simulations is in agreement with the large growth rates of the interior mode. The lateral scales of MLI are set by the Rossby radius given by the stratification and depth of the ML and consequently much smaller than the lateral scales of the interior mode. Our shallow mode corresponds to the MLI of Boccaletti et al. (2007) and has indeed larger growth rates than the interior mode.

Both shallow and interior mode are called balanced modes and are related to the Rossby wave branch (in contrast to the unbalanced gravity wave branch). Based on the orientation of the wavenumber vector in flow direction, and on the form of the growth rate as a function of wavenumber, it is clear that the interior and the shallow mode are Eady-type baroclinic instabilities, as discussed by many authors before (e.g. Stone 1970). However, it is also clear that ageostrophic terms are not small in particular for the dynamics of the shallow mode, since the Ri becomes $O(1)$. In any case, the shallow mode is different from the ageostrophic mode by Molemaker et al. (2005) which can also be found in the mixed layer, and which is clearly out of balance, as detailed in the introduction.

Low Richardson numbers well below 10 within the upper LC in March result in three times larger growth rates of the interior mode compared to September. The low Richardson numbers result from a combination of weak stratification and enhanced vertical shear in winter, which are in turn related to a combination of local buoyancy loss and the advection of weakly stratified denser convective water masses from the interior. During the rest of the year strong stratification and weak vertical shear lead to larger Richardson numbers and smaller growth rates. Since larger isopycnal slopes and vertical shear, and weak stratification in winter are indeed observed features of the LC (Pickart et al. 2002; Cuny et al. 2005), our analysis suggests that the interior mode with increased growth rates due to low Richardson numbers leads to the observed EKE maximum in the LC in winter.

Using the scaling of the velocity amplitudes introduced in Killworth (1997); Eden (2011), the interior mode contains most of the kinetic energy, since it has a much larger wavelength than the shallow mode, which compensates the smaller growth rate of the interior mode. The scaling can thus explain why a great portion of the observed variance in the LC due to baroclinic instability is also present in the model simulations. On the other hand, we speculate that the missing variance in the model simulation compared to observations might result from EKE related to the unresolved shallow mode, but this can only be answered by increasing the model resolution well below 1 km. Based on the scaling of the velocity amplitudes, we might also speculate that the more energetic interior mode is more important for lateral mixing and stirring than the less energetic shallow mode. However, linear stability analysis does not allow to infer the mixing effects of the instabilities in the fully non-linear turbulent regime.

The symmetric mode also does not show up in the model, but we do not expect this mode to be important for lateral mixing and stirring. However, it does modify convection in the LC to slantwise convection (e.g. Cuny et al. 2005). We have not found the ageostrophic, unbalanced mode described by Stone (1971); Molemaker et al. (2005) in the linear stability analysis, since it has always smaller growth rates than the balanced modes. This mode might play an important role for the dissipation of kinetic energy of the mean balanced flow, but because of the smaller growth rates, we do not expect this mode to play an important role for lateral mixing.

Since our model simulation is climatologically forced we cannot realistically account for interannual variability. The growth rate of the instability process depends on the Richardson number, which depends in turn to some extent on the watermasses advected from the interior of the Labrador Sea. Since the deep convection activity and thus the stratification in the Labrador Sea shows large interannual variability (e.g. Lazier et al. 2002), it is possible that the strength of the instability process also shows large interannual variability. Thus, model simulations with realistic interannually varying forcing are suggested in order to learn about the possible linkage between the strength of deep convection and the instability process in the boundary current.

Finally, a few caveats need to be addressed: The linear stability analysis accounts only for vertical shear instability, while horizontal shear and thus barotropic instability is not included. Eden and Böning (2002) calculated energy transfer rates of potential energy and kinetic energy of the mean flow into the EKE along the LC, and find that generally only 10% of the EKE is fed from the lateral shear of the mean flow. It thus seems to be sufficient here to focus on the vertical shear only. For other boundary currents such as the shelf break current in the Mid Atlantic bight, lateral shear appear to be more important (Lozier et al. 2002). The LC is certainly also influenced by topography, but topographic effects are neglected here. Since the focus of this study lies on seasonal effects and the topography does not change during the year, this simplification seems justified. Furthermore, (Lozier and Reed 2005) found that for baroclinic currents, the effect of topography remains small. On the other hand, topography can also stabilize currents (Isachsen 2011; Vollmer and Eden

2013), such that growth rates might be overestimated.

Acknowledgments

We thank Jürgen Fischer and Rainer Zantopp for providing the moored current datasets, and two reviewers for their help to improve the manuscript.

Appendix A

The linear stability analysis is based on the following equations:

$$\partial_t \boldsymbol{u} + \boldsymbol{u} \cdot \boldsymbol{\nabla} \boldsymbol{u} = -\boldsymbol{\nabla} p + 2\boldsymbol{\Omega} \times \boldsymbol{u} + b\boldsymbol{e}_z + A_v \partial_{zz} \boldsymbol{u} + A_h \boldsymbol{\nabla}^2 \boldsymbol{u} \quad (1)$$

$$\partial_t b + \boldsymbol{u} \cdot \boldsymbol{\nabla} b = K_v \partial_{zz} b \quad (2)$$

$$\partial_t p + c_s^2 \boldsymbol{\nabla} \cdot \boldsymbol{u} = 0 \quad (3)$$

where $\boldsymbol{u}$ denotes the fluid particle velocity, p the (scaled) pressure, b the buoyancy, $\boldsymbol{\Omega} = |\boldsymbol{\Omega}|(0, \cos\phi, \sin\phi)$ the Earth rotation vector at latitude ϕ, c_s the speed of sound, $\boldsymbol{e}_z$ the vertical unit vector, A_v and A_h vertical and horizontal viscosities, respectively, and K_v vertical diffusivity. The Boussinesq approximation is applied to the momentum Eq. (1) and full incompressibility (or $c_s \to \infty$) was assumed to derive Eq. (2) by combining temperature and salt conservation equations. Eq. (3) is a combination of mass conservation and the equation of state (see e.g. Olbers et al. 2012), where the Boussinesq approximation is only partially applied by keeping a finite c_s in the time derivative of p, which makes it a prognostic equation for p. By doing so, it is much simpler to obtain the eigensolutions of the linearized system by numerical methods, as for the fully incompressible equations considered by e.g. Stone (1971). On the other hand, sound waves will be part of the solution, but they can easily be identified by their large phase velocities and sorted out, even when artificially decreasing c_s. We found this method to work well for $c_s = 150\,m/s$, the value which we use in this study, and we do not expect any effects of the sound waves on the remaining (gravity and Rossby) wave branches, since tests with variations in c_s do not change the solution and analytical solutions of idealized test cases as the Eady case are correctly reproduced.

The equations are linearized with respect to a basic state with vanishing vertical velocity, and no horizontal variations in lateral velocity and stratification, using $w = 0$ and $\partial p/\partial z = 0$ at $z = -h, 0$ as kinematic and dynamic boundary conditions. By ignoring lateral variations of the background flow and stratification, we do not account for lateral shear instability and assume that those instabilities are unimportant for the purpose of this study. For a non-constant Earth rotation vector $\boldsymbol{\Omega}$ in Eq. (1), linear waves do not solve the problem. A streamfunction and velocity potential is therefore introduced for the horizontal velocity. In the corresponding tendency equations for streamfunction and velocity potential, $\boldsymbol{\Omega}$ and $d\boldsymbol{\Omega}/dy$ show up and are taken both as constants, to allow for a varying $\boldsymbol{\Omega}$ (in a WKB sense).

For wave solutions $\boldsymbol{u} = \boldsymbol{u}_0(z) \exp i(\boldsymbol{k} \cdot \boldsymbol{x} - \omega t)$, $b = b_0(z) \exp i(\boldsymbol{k} \cdot \boldsymbol{x} - \omega t)$, and $p = p_0(z) \exp i(\boldsymbol{k} \cdot \boldsymbol{x} - \omega t)$, with the horizontal wave number vector $\boldsymbol{k} = (k, l)$ and the frequency ω, Eq. (1) to Eq. (3) become a vertical eigenvalue equation. Discretization in the vertical yields an algebraic eigenvalue problem, which can be solved at given k and l for the vertical eigenfunctions $\boldsymbol{u}_0$, b_0, p_0, and the eigenvalues ω. $\mathrm{Im}(\omega)$ is the growth rate of the solution; we consider only eigenfunctions with the largest growth rate at given k and l. $\mathrm{Re}(\omega)/|\boldsymbol{k}|$ is the phase velocity, the related EKE is given by $\mathrm{Re}(\boldsymbol{u}_0 \cdot \boldsymbol{u}_0^*)/2$.

REFERENCES

Barnier, B., L. Siefridt, and P. Marchesiello, 1995: Thermal forcing for a global ocean circulation model using a three year climatology of ECMWF analysis. *J. Mar. Sys.*, **6**, 363–380.

Beckmann, A. and R. Döscher, 1997: A method for improved representation of dense water spreading over topography in geopotential-coordinate models. *J. Phys. Oceanogr.*, **27**, 581–591.

Boccaletti, G., R. Ferrari, and B. Fox-Kemper, 2007: Mixed layer instabilities and restratification. *J. Phys. Oceanogr.*, **37**(9), 2228–2250.

Brandt, P., A. Funk, L. Czeschel, C. Eden, and C. W. Böning, 2007: Ventilation and transformation of Labrador Sea Water and its rapid export in the deep Labrador Current. *J. Phys. Oceanogr.*, **37**, 946–961.

Brandt, P., F. Schott, A. Funk, and C. S. Martins, 2004: Seasonal to interannual variability of the eddy field in the Labrador Sea from satellite altimetry. *J. Geophys. Res.*, **109**, C02028.

Chelton, D. B., M. G. Schlax, R. M. Samelson, and R. A. de Szoeke, 2007: Global observations of large oceanic eddies. *J. Geophys. Res.*, **34**(15).

Cuny, J., P. B. Rhines, P. P. Niiler, and S. Bacon, 2002: Labrador Sea boundary currents and the fate of the Irminger Sea Water. *J. Phys. Oceanogr.*, **32**(2), 627–647.

Cuny, J., P. B. Rhines, F. Schott, and J. Lazier, 2005: Convection above the Labrador Continental Slope. *J. Phys. Oceanogr.*, **35**(4), 489–511.

Czeschel, L., 2005: *The role of eddies for the deep water formation in the Labrador Sea*. Ph.D. thesis, Christian-Albrechts-Universität, Kiel, Germany.

Eady, E. T., 1949: Long waves and cyclone waves. *Tellus*, **1**(3), 33–52.

Eden, C., 2011: A closure for meso-scale eddy fluxes based on linear instability theory. *Ocean Modelling*, **39**(3–4), 362–369.

Eden, C., 2012: Implementing diffusivities from linear stability analysis in a three-dimensional general circulation ocean model. *Ocean Modelling*, **57**, 15–28.

Eden, C. and C. Böning, 2002: Sources of eddy kinetic energy in the Labrador Sea. *J. Phys. Oceanogr.*, **32**(12), 3346–3363.

Fischer, J., F. A. Schott, and M. Dengler, 2004: Boundary circulation at the exit of the Labrador Sea. *J. Phys. Oceanogr.*, **34**(7), 1548–1570.

Fratantoni, D. M., 2001: North Atlantic surface circulation during the 1990's observed with satellite-tracked drifters. *J. Geophys. Res.*, **106**, 22067–22093.

Gaspar, P., Y. Gregoris, and J.-M. Lefevre, 1990: A simple eddy kinetic energy model for simulations of the oceanic vertical mixing: Tests at Station Papa and long-term upper ocean study site. *J. Geophys. Res.*, **95**(C9), 16179–16193.

Haine, T. W. N. and J. Marshall, 1998: Gravitational, symmetric, and baroclinic instability of the ocean mixed layer. *J. Phys. Oceanogr.*, **28**, 634–658.

Haney, R. L., 1971: Surface thermal boundary condition for ocean circulation models. *J. Phys. Oceanogr.*, **1**, 79–93.

Isachsen, P., 2011: Baroclinic instability and eddy tracer transport across sloping bottom topography: How well does a modified Eady model do in primitive equation simulations? *Ocean Modelling*, **39**(1), 183–199.

Killworth, P., 1997: On the parameterization of eddy transfer Part I. Theory. *J. Mar. Res.*, **55**(6), 1171–1197.

Kraus, E. B. and J. S. Turner, 1967: A one-dimensional model of the seasonal thermocline. II, the general theory and its consequences. *Tellus*, **19**, 98–105.

Lavender, K. L., R. E. Davis, and W. B. Owens, 2002: Observations of open-ocean deep convection in the Labrador Sea from subsurface floats. *J. Phys. Oceanogr.*, **32**, 511–526.

Lazier, J., 1973: The renewal of Labrador Sea Water. *Deep-Sea Res.*, **20**(4), 341 – 353.

Lazier, J., R. Hendry, A. Clarke, I. Yashayaev, and P. Rhines, 2002: Convection and restratification in the Labrador Sea, 1990–2000. *Deep-Sea Res.*, **49**(10), 1819–1835.

Lazier, J. R. N. and D. G. Wright, 1993: Annual velocity variations in the Labrador Current. *J. Phys. Oceanogr.*, **23**, 659–678.

Levitus, S. and T. P. Boyer, 1994: World Ocean Atlas 1994. Technical report, NOAA, U.S. Gov. Print. Off., Washington D.C,USA.

Lozier, M. S. and M. S. C. Reed, 2005: The influence of topography on the stability of shelfbreak fronts. *J. Phys. Oceanogr.*, **35**(6), 1023–1036.

Lozier, M. S., M. S. C. Reed, and G. G. Gawarkiewicz, 2002: Instability of a shelfbreak front. *J. Phys. Oceanogr.*, **32**(3), 924–944.

Marshall, J., A. Adcroft, C. Hill, L. Perelman, and C. Heisey, 1997: A finite-volume, incompressible Navier Stokes model for studies of the ocean on parallel computers. *J. Geophys. Res.*, **102**, 5753–5766.

Marshall, J. and F. Schott, 1999: Open-ocean convection: Observations, theory, and models. *Rev. Geophys.*, **37**(1), 1–64.

Molemaker, M. J., J. C. McWilliams, and I. Yavneh, 2005: Baroclinic instability and loss of balance. *J. Phys. Oceanogr.*, **35**, 1505.

Molemaker, M. J., M. J., J. C. McWilliams, and X. Capet, 2010: Balanced and unbalanced routes to dissipation in an equilibrated Eady flow. *J. Fluid Mech.*, **654**, 35–63.

Morsdorf, F., 2001: *Randstromvariabilität in der Labradorsee*. Master's thesis, Christian-Albrechts-Universität, Kiel, Germany.

Munk, W., L. Armi, K. Fischer, F. Zachariasen, W. Munk, L. Armi, K. Fischer, and F. Zachariasen, 2000: Spirals on the sea. *Proceedings of the Royal Society of London. Series A: Mathematical, Physical and Engineering Sciences*, **456**(1997), 1217–1280.

Olbers, D., J. Willebrand, and C. Eden, 2012: *Ocean Dynamics*. Springer, Heidelberg.

Palter, J. B., M. S. Lozier, and K. L. Lavender, 2008: How does Labrador Sea Water enter the Deep Western Boundary Current? *J. Phys. Oceanogr.*, **38**(5), 968–983.

Pickart, R. S., D. J. Torres, and R. A. Clarke, 2002: Hydrography of the Labrador Sea during Active Convection. *J. Phys. Oceanogr.*, **32**, 428–457.

Rattan, S., Myers, P. G., Treguier, A-M., Theetten, S., Biastoch, A. and Böning, C., 2010: Towards an understanding of Labrador Sea salinity drift in eddy-permitting simulations. *Ocean Modelling*, **35**(1), 77–88.

Schott, F., L. Stramma, R. J. Zantopp, M. Dengler, J. Fischer, and M. Wibaux, 2004: Circulation and deep water export at the western exit of the subpolar North Atlantic. *J. Phys. Oceanogr.*, **34**, 817–843.

Smith, K. and J. Marshall, 2009: Evidence for enhanced eddy mixing at middepth in the Southern Ocean. *J. Phys. Oceanogr.*, **39**(1), 50–69.

Smith, K. S., 2007: The geography of linear baroclinic instability in Earth's oceans. *J. Mar. Res.*, **65**(5), 655–683.

Spall, M. A., 2010: Dynamics of downwelling in an eddy-resolving convective basin. *J. Phys. Oceanogr.*, **40**(10), 2341–2347.

Stevens, D. P., 1990: On open boundary conditions for three dimensional primitiv equation ocean circulation models. *Geophys. Astrophys. Fluid Dyn.*, **51**, 103–133.

Stone, P. H., 1966: On non-geostrophic baroclinic stability. *J. Atmos. Sci.*, **23**(4), 390–400.

Stone, P. H., 1970: On non-geostrophic baroclinic stability: Part II. *J. Atmos. Sci.*, **27**, 721–726.

Stone, P. H., 1971: Baroclinic stability under non-hydrostatic conditions. *J. Fluid Mech.*, **45**(04), 659–671.

Thomas, L. N., A. Tandon, and A. Mahadevan, 2008: *Submesoscale processes and dynamics*, volume 177, pp. 17–38. AGU, Washington, DC. ISBN 978-0-87590-442-9.

Treguier, A., I. Held, and V. Larichev, 1997: Parameterization of quasigeostrophic eddies in primitive equation ocean models. *J. Phys. Oceanogr.*, **27**(4), 567–580.

Treguier, A. M., S. Theetten, E. P. Chassignet, T. Penduff, R. Smith, L. Talley, J. O. Beismann, and C. Böning, 2005: The North Atlantic subpolar gyre in four high-resolution models. *J. Phys. Oceanogr.*, **35**, 757.

Vollmer, L. and C. Eden, 2013: A global map of meso-scale eddy diffusivities based on linear stability analysis. *Ocean Modelling* (in press).

White, M. A. and K. J. Heywood, 1995: Seasonal and interannual changes in the North Atlantic subpolar gyre from Geosat and TOPEX/Poseidon altimetry. *J. Geophys. Res.*, **100**(C12), 24931–24941.

Yashayaev, I., M. Bersch, and H. M. van Aken, 2007: Spreading of the Labrador Sea Water to the Irminger and Iceland basins. *Geophys. Res. Letters*, **34**(10).

List of Tables

Month	Jan	Feb	Mar	Apr	May	Jun	Jul	Aug	Sep	Oct	Nov	Dec
Im(ω) in d^{-1}, interior	0.81	0.85	0.94	0.50	0.73	0.18	0.22	0.34	0.34	0.34	0.69	0.76
Im(ω) in d^{-1} shallow	3.36	3.06	3.03	3.13	3.49	3.47	3.47	3.05	3.30	2.66	3.30	2.95
L in km, interior	39	46	43	30	35	33	39	41	42	43	34	30
L in km, shallow	1.5	2.3	1.8	0.4	0.6	0.4	0.4	0.3	0.3	0.6	1.2	0.9

TABLE 1. Growth rate Im(ω) and wavelength L of the interior and shallow mode at K6 from monthly mean background shear and stratification from FLAME. U and V at velocity grid points closest to the mooring positions and N^2 interpolated on these points are taken as background values for the linear stability analysis.

List of Figures

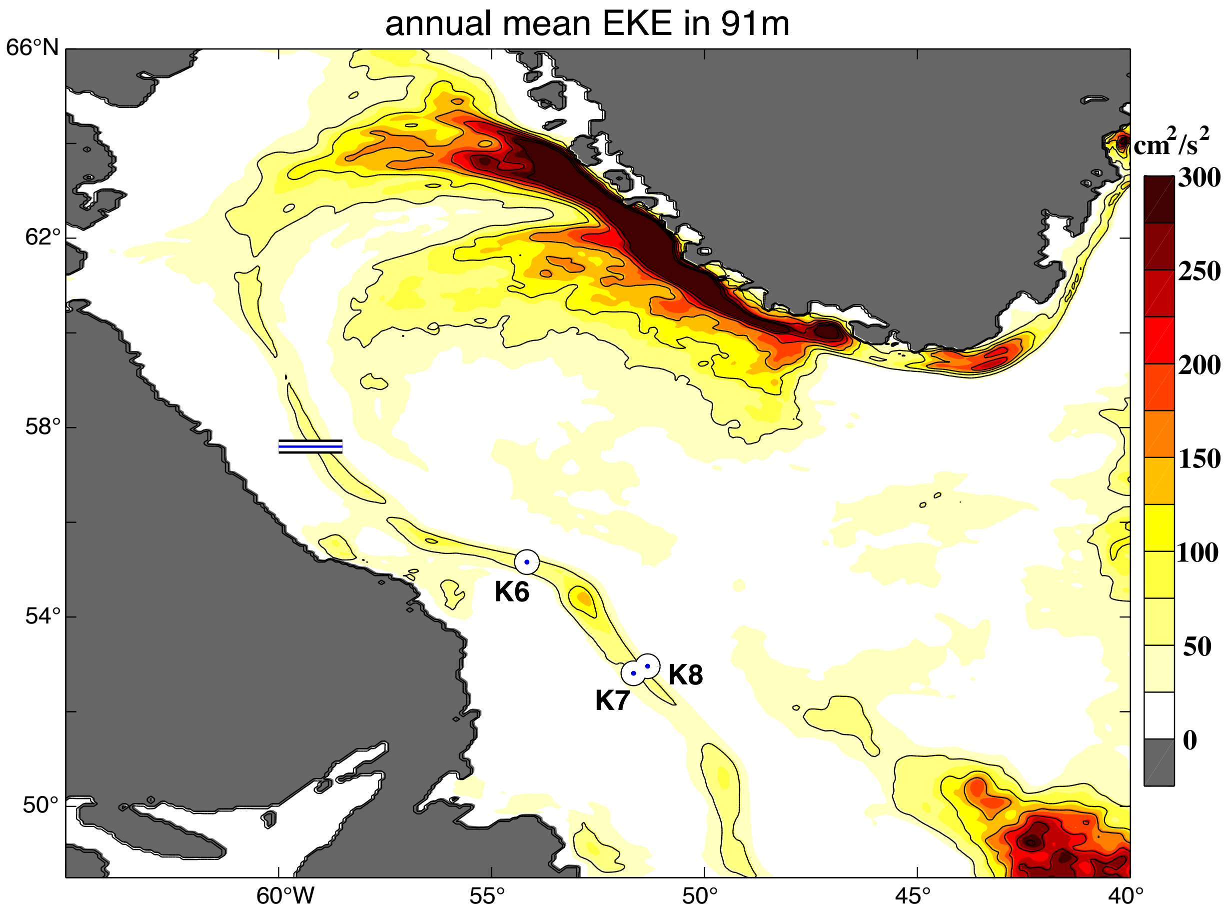

Fig. 1. Annual mean EKE in $\mathrm{cm^2/s^2}$ in the LS, calculated from three years of the MITGCM simulation. The contour interval is $50\,\mathrm{cm^2/s^2}$. EKE is calculated using velocity deviations from a seasonal mean using three years of model data. u and v have been interpolated on tracer grid points prior to the analysis. White circles denote the position of the upstream mooring K6, and the downstream moorings K7 and K8. Bars indicate the section shown in Fig. 9.

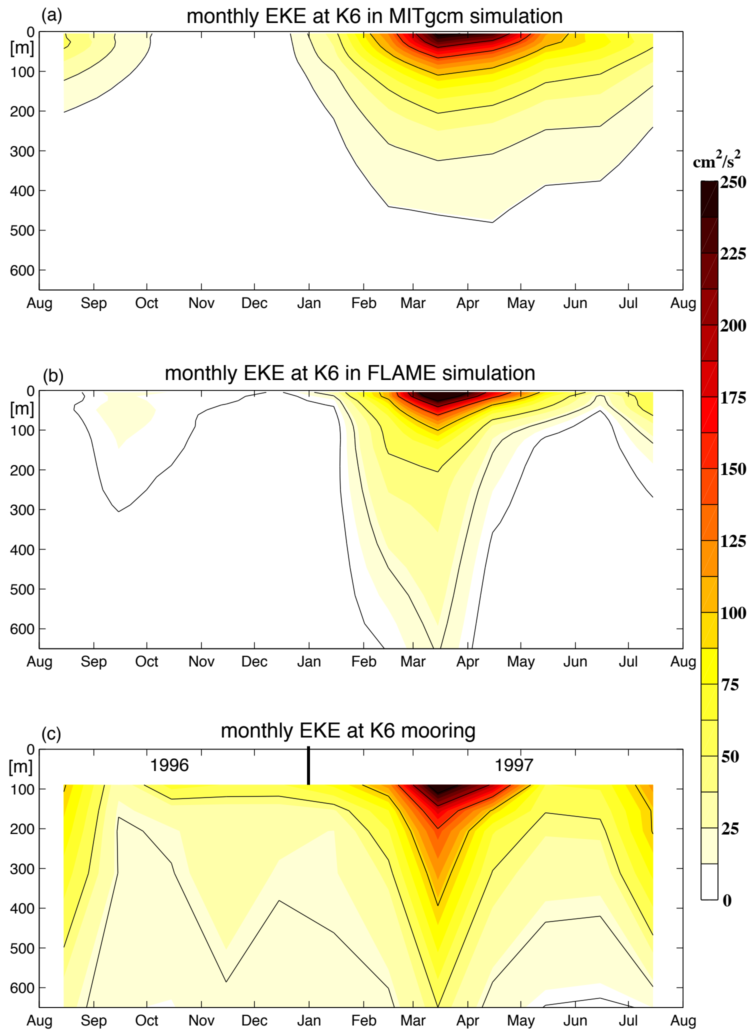

Fig. 2. Monthly mean EKE in cm^2/s^2 at K6 in MITGCM (a), FLAME (b) and moored current data (c). EKE is calculated using band-pass (2 to 30 d) filtered velocity using three (one) years of model data from MITGCM (FLAME) and from one year mooring data. The EKE of the observational current data is estimated at five different depths (at around 90, 155, 205, and 310 m from ADCP data and around 660 m from RCM data). The black contour lines indicate 10, 20, 50, 100, 150, 200 and 250 cm^2/s^2. The mooring does not cover the upper 100 m due to surface reflection and vertical mooring displacement. u and v in MITGCM have been interpolated on tracer grid points prior to the analysis. EKE at grid points closest to the mooring positions are shown in a) and b).

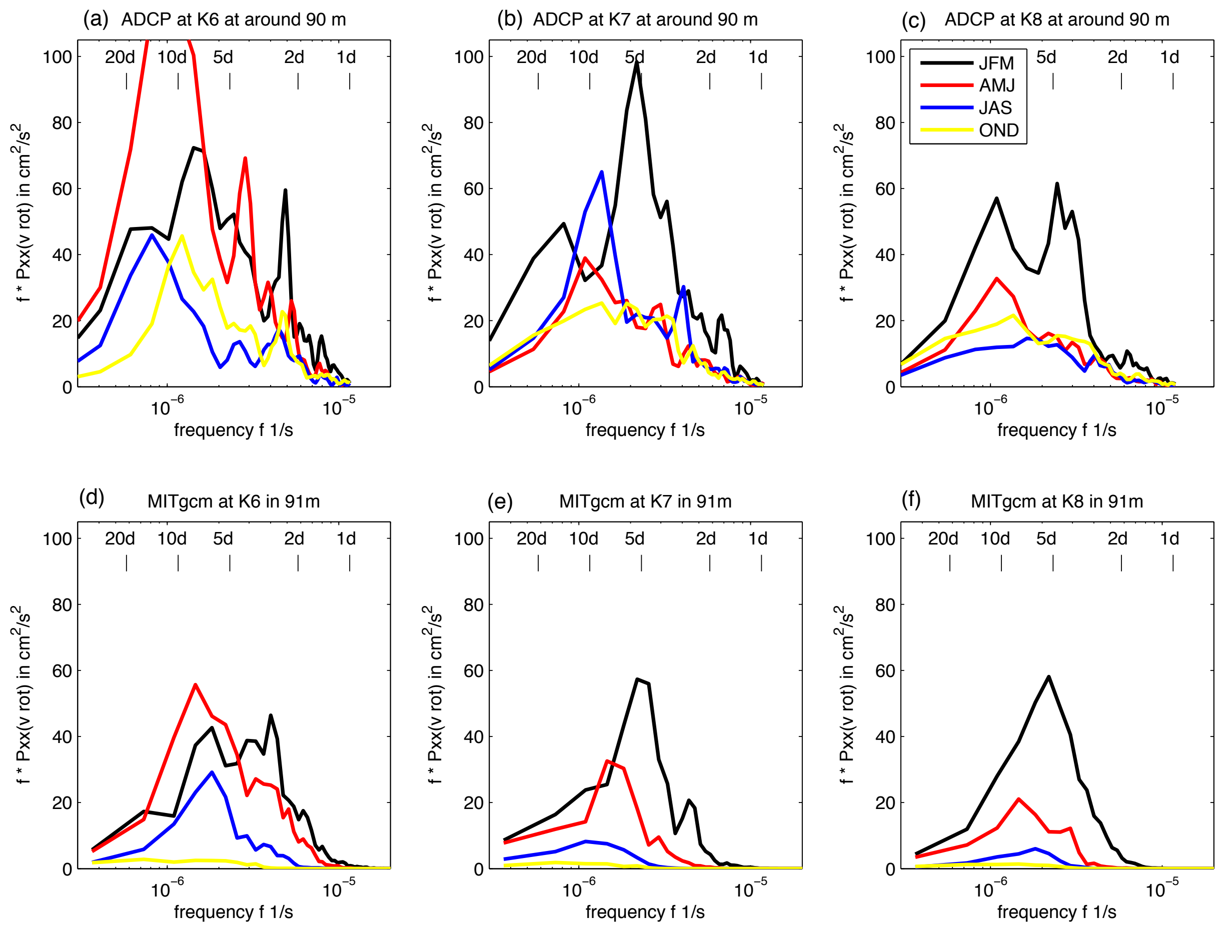

FIG. 3. Variance-preserving spectra of the alongshore flow for different moorings (K6, K7 and K8, for exact location see Fig. 1) estimated from moored ADCP data (a),(b) and (c) (from one, two and two years in a,b,c, respectively) as well as from three years MITGCM simulation (d),(e) and (f). The data was cut into 30 day segments, with 15 days overlap. Each segment was detrended and multiplied with a hamming window. All segments within one season are averaged. Winter (JFM) in black, spring (AMJ) in red, summer (JAS) in blue and autumn (OND) in yellow. Tides and internal waves are removed from the ADCP current data with a 40 hours low-pass filter. u and v in MITGCM have been interpolated on the tracer grid points closest to the respective mooring position prior to the analysis.

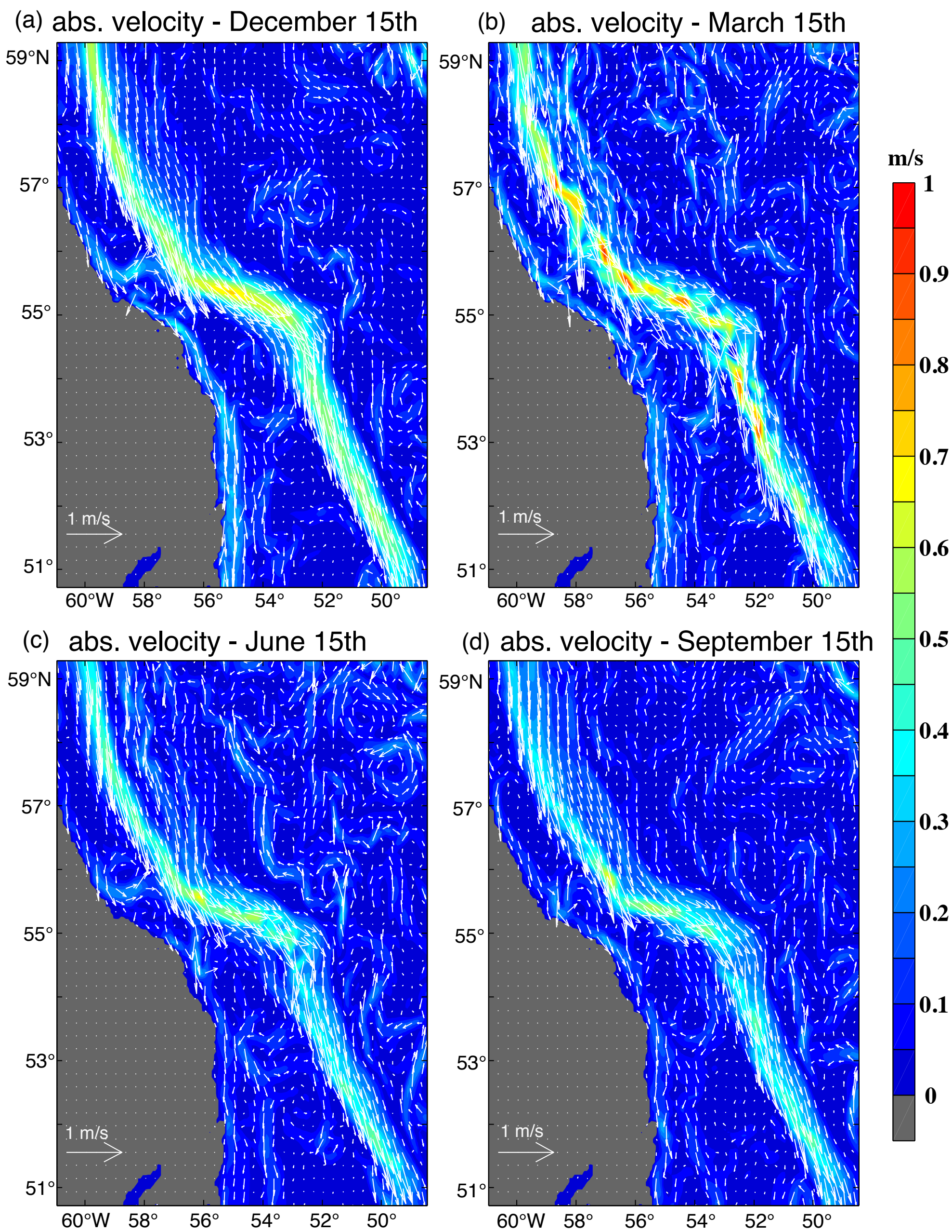

FIG. 4. Instantaneous snapshots of speed and velocity (arrows, every fourth grid point) at 91 m depth in the MITGCM simulation for four different times of the year in the southwestern LS. (a) December 15th, (b) March 15th, (c) June 15th and (d) September 15th. u and v have been interpolated on tracer grid points prior to the analysis.

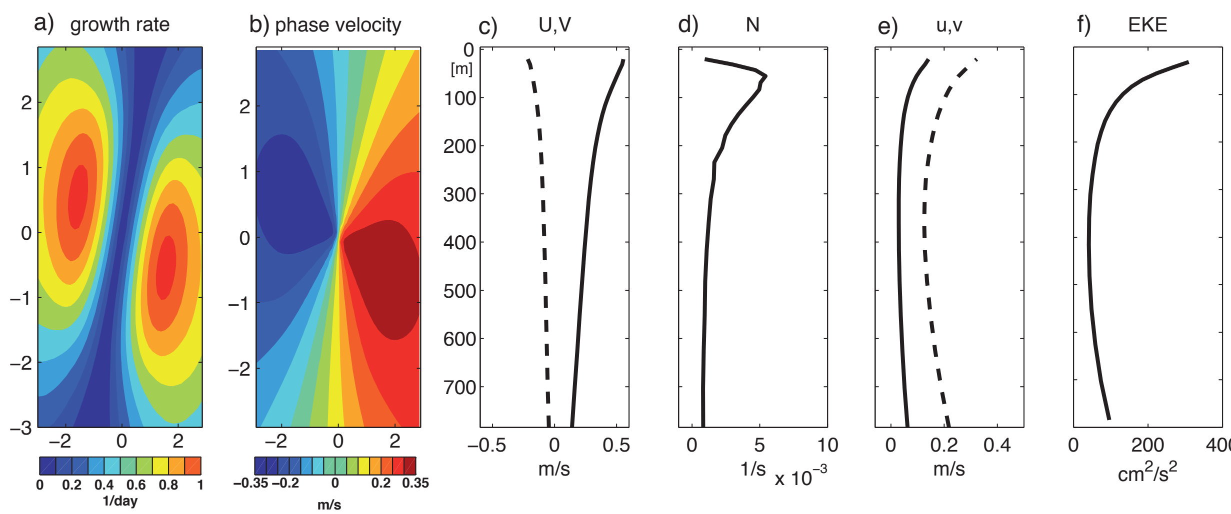

FIG. 5. The interior mode at K6 calculated from March mean background shear and stratification from FLAME. Shown are the growth rate in 1/day (a) and the phase velocity in m/s (b) as a function of the (scaled) wave numbers. The wave numbers are scaled using the local Rossby radius $\int_{-h}^{0} N/f dz$. Monthly mean background velocity U (solid) and V in m/s (dashed) (c) and stratification N in 1/s (d) are also shown together with the vertical structure functions of the predicted perturbation velocities u (solid) and v (dashed) in m/s (e) and the resulting EKE $((u^2+v^2)/2)$ in cm^2/s^2 (f) for the fastest growing mode. U and V at velocity grid points closest to the mooring positions and N^2 interpolated on these points are taken as background values.

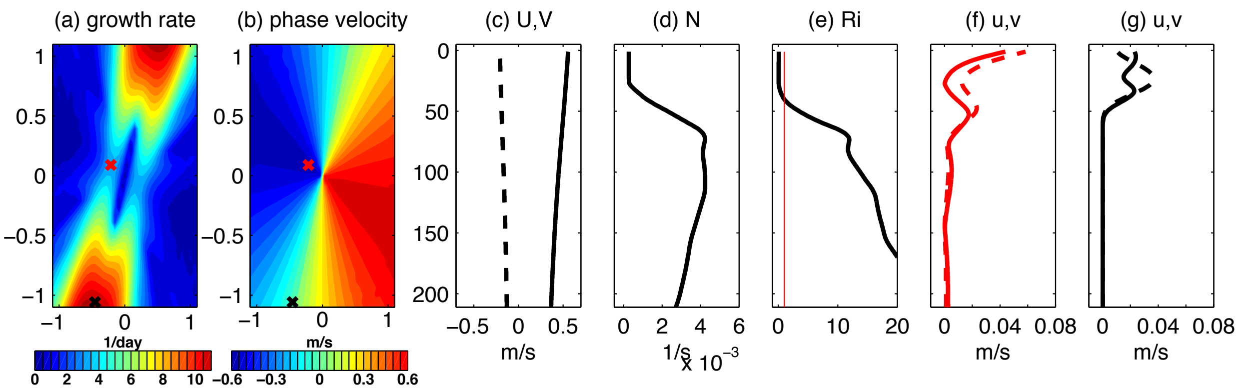

FIG. 6. The shallow (red cross in a and b) and symmetric mode (black cross in a and b) at K6 for background shear and stratification taken from January mean values in FLAME. Shown are the growth rate in 1/day (a), phase velocity in m/s (b), monthly mean background velocities U (solid) and V (dashed) in m/s (c), and the background stratification N in 1/s (d). The Richardson number Ri is shown in (e) as black solid line, the red line indicates $Ri = 1$. Velocity perturbations u (solid) and v (dashed) of the shallow mode in m/s are shown in (f), the corresponding variables for the symmetric mode are shown in (g). The corresponding growth rates for the shallow and symmetric mode are marked with a red and black cross in a) and b), respectively. The wave numbers in a) and b) are scaled with the mixed layer Rossby radius (see text for definition). U and V at velocity grid points closest to the mooring positions and N^2 interpolated on these points are taken as background values.

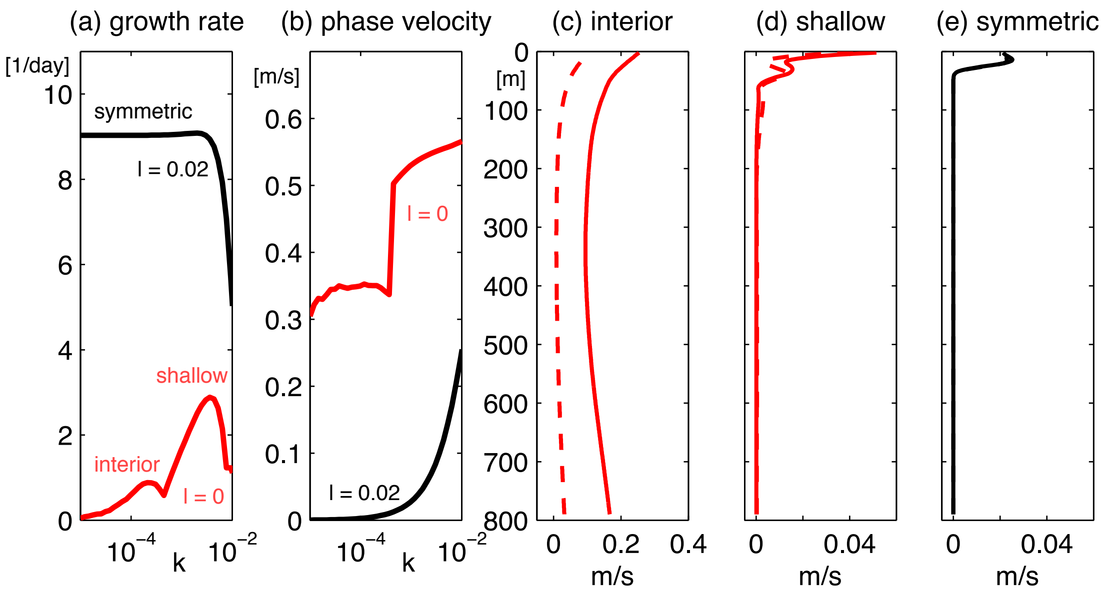

FIG. 7. Interior, shallow and symmetric mode at K6 for background shear and stratification taken from March mean values in FLAME. Shown are the growth rate in 1/day (a) and phase velocity in m/s (b) as a function of the along-flow wavenumber k in $1/m$ for cross-flow wavenumber $l = 0$ (black) and $l = 0.02/m$ (red). U and V at velocity grid points closest to the mooring positions and N^2 interpolated on these points are taken as background values. The background flow and planetary vorticity gradient are rotated by 22 degrees in anticlockwise direction, such that V becomes minimal. c), d) and e) show the eigenfunctions of u and v for the different modes.

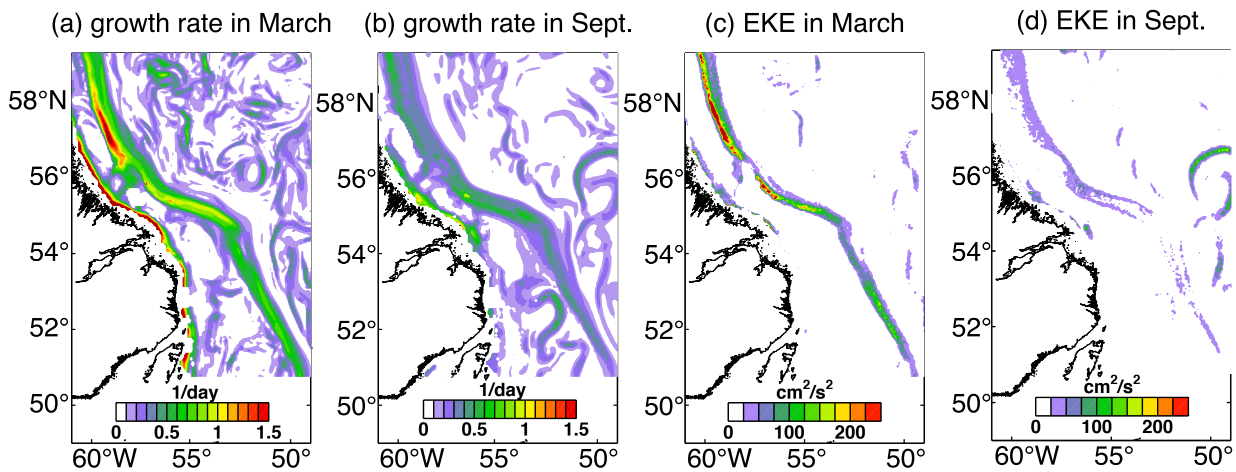

FIG. 8. Predicted growth rates in FLAME in 1/day (a,b) of the interior mode, and its related EKE at around 100 m depth in cm^2/s^2 (c,d) during March (a,c) and September (b,d) in the southwestern LS. U and V at velocity grid points and N^2 interpolated on these points are taken as background values.

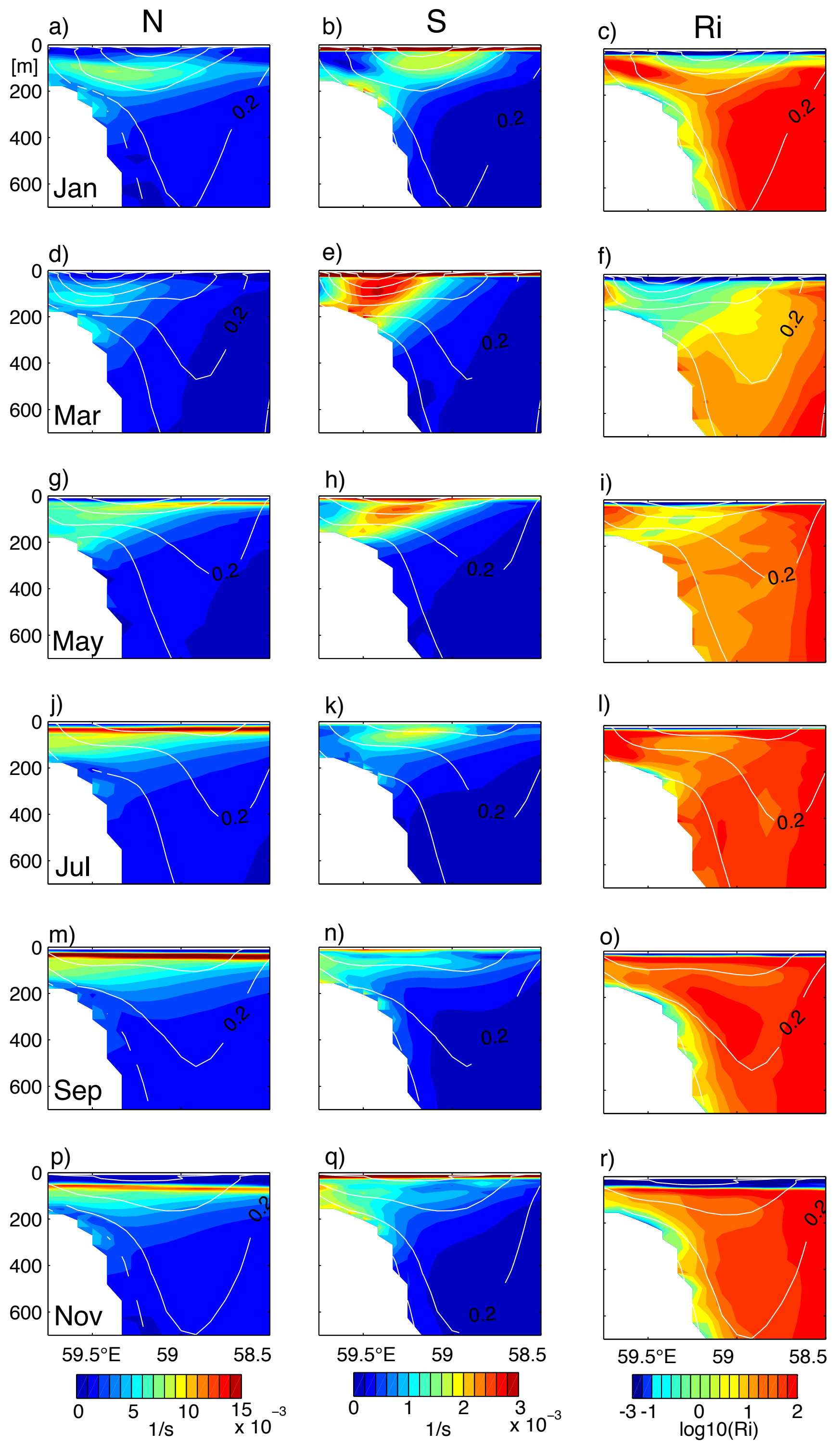

FIG. 9. Seasonal cycle of monthly mean buoyancy frequency N in 1/s, vertical shear $S = \sqrt{(\partial u/\partial z)^2 + (\partial v/\partial z)^2}$ in 1/s and the logarithm of the Richardson number $Ri = N^2/S^2$ along 57.6^{o}N from FLAME. Also shown is the alongshore velocity component (solid white lines in m/s with contour interval of 0.1 m/s)